

Melt-Quenched Glasses of Metal-Organic Frameworks

Thomas D. Bennett^{†,*}, Yuanzheng Yue^{§,†}, Peng Li[⊥], Ang Qiao[§], Haizheng Tao[§], Neville G. Greaves^{†,§,||}, Tom Richards[†], Giulio I. Lampronti[▽], Simon A. T. Redfern[▽], Frédéric Blanc[#], Omar K. Farha[⊥], Joseph T. Hupp[⊥], Anthony K. Cheetham[†] and David A. Keen[○]

[†] Department of Materials Science and Metallurgy, University of Cambridge, 27 Charles Babbage Road, Cambridge, CB3 0FS, UK.

[§] State Key Laboratory of Silicate Materials for Architectures, Wuhan University of Technology, Wuhan 430070, China.

[‡] Department of Chemistry and Bioscience, Aalborg University, DK-9220 Aalborg, Denmark.

[⊥] Department of Chemistry and International Institute for Nanotechnology, Northwestern University, Evanston, USA

^{||} Institute of Mathematics, Physics and Computer Science, Aberystwyth University, Aberystwyth, SY23 3BZ, UK.

[▽] Department of Earth Sciences, University of Cambridge, Downing Street, Cambridge, CB2 3EQ, UK.

[#] Department of Chemistry and Stephenson Institute for Renewable Energy, University of Liverpool, Crown Street, Liverpool, L69 7ZD, UK.

[○] ISIS Facility, Rutherford Appleton Laboratory, Harwell Oxford, Didcot, Oxon, OX11 0QX, UK.

Crystalline solids dominate the field of metal-organic frameworks (MOFs), with access to the liquid and glass states of matter usually prohibited by relatively low temperatures of thermal decomposition. In this work, we give due consideration to framework chemistry and topology to expand the phenomenon of the melting of three-dimensional MOFs, linking crystal chemistry to framework melting temperature and kinetic fragility of the glass-forming liquids. Here we show that melting temperatures can be lowered by altering the chemistry of the crystalline MOF state, which provides a route to facilitate the melting of other MOFs. The glasses formed upon vitrification are chemically and structurally distinct from the three other existing categories of melt-quenched glasses (inorganic non-metallic, organic and metallic), and retain the basic metal-ligand connectivity of crystalline MOFs, which connects their mechanical properties to starting chemical composition. The transfer of functionality from crystal to glass points towards new routes to tunable, functional hybrid glasses.

Introduction

The synthesis of crystalline metal-organic frameworks (MOFs) for gas sorption and separation, catalysis, drug delivery, conductive and multiferroic applications is widespread.¹⁻⁴ These network materials consist of metal nodes linked by organic ligands in infinite arrays and are heralded for their chemical versatility in being able to accommodate an enormous range of ligand- or metal-based functionalities.⁵⁻⁹ A family of MOFs, known as zeolitic imidazolate frameworks (ZIFs), is of particular interest given their chemical stability and structural similarities to classical zeolite networks.^{10,11} ZIFs have significantly ‘softer’ mechanical properties compared to their inorganic cousins,¹²⁻¹⁴ and may structural collapse upon heating, pressurization or ball-milling¹⁵ to form amorphous frameworks which possess the same short-range connectivity as their crystalline counterparts.¹⁶

Certain one and two-dimensional coordination polymers exhibit transitions between solid and glass-like states^{17,18} as does one three-dimensional MOF, ZIF-4 [Zn(Im)₂] (Im – imidazolate, C₃H₃N₂).¹⁹ These appear different from other melt-quenched glasses (MQGs), which are divided according to their underlying chemistry into inorganic non-metallic (e.g. oxide and chalcogenide glasses), organic (e.g. polymer glasses) and metallic categories.²⁰ Importantly, the MQGs here are distinct from the sol-gel derived hybrid amorphous solids reported by Novak,²¹ which are produced via partial hydrolysis and subsequent condensation of metal alkoxides modified with an organic moiety (e.g. Si(OR)₄). Such MOF-glasses (our term for MQGs produced by quenching molten MOFs) form as a result of the freezing-in of the melt structure.

Table 1: Compositions, melting and glass transition temperatures of the glasses, along with liquid fragilities and crystalline porosities.

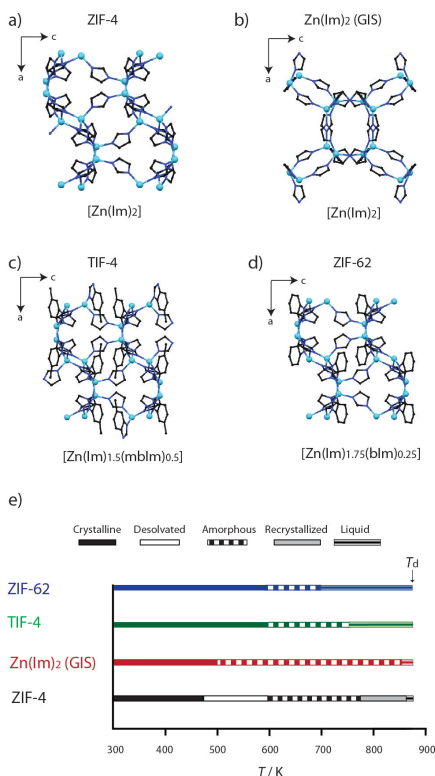
Sample	Composition	Porosity (P) / % ^[a]	Melting Point / K	Glass Transition / K	Fragility (m) ^[b]
ZIF-4	Zn(Im) ₂	23.6	863	565	39 (41) ¹⁹
Zn(Im) ₂	Zn(Im) ₂	56.9	857	565 (560)	17 (15)

(GIS)

TIF-4	$\text{Zn}(\text{Im})_{1.5}(\text{mbIm})_{0.5}$	18.6	740	616	23
ZIF-62	$\text{Zn}(\text{Im})_{1.75}(\text{bIm})_{0.25}$	22.5	710	591	35

^[a] Crystalline porosities calculated using the Mercury software with a probe radius of 1.2 Å and a grid spacing of 0.7 Å. ^[b] Fragilities of $a\tau\text{ZIF-4}$ and $a\tau\text{Zn}(\text{Im})_2$ (GIS), and the glass transition temperature for $a\tau\text{Zn}(\text{Im})_2$ (GIS) are italicized and in brackets, where appropriate.

Figure 1. Unit cells viewed along the *b* axis of (a) ZIF-4, (b) $\text{Zn}(\text{Im})_2$ (GIS), (c) TIF-4 and (d) ZIF-62. N – dark blue, Zn – light blue, C – black, H – omitted. (e) Schematic of the thermal events on heating. Differences in behavior are evident, with $\text{Zn}(\text{Im})_2$ (GIS), TIF-4 and ZIF-62 undergoing amorphization upon desolvation, and a large temperature range between melting and framework decomposition for



Motivated by the unique opportunities offered by transferring the chemical functionality of crystalline MOFs to thermo-mechanically stable glasses with tunable inorganic and organic components,²² we present a detailed investigation of the phenomenon of MOF melting in several three-dimensional framework structures.

Pair distribution function (PDF) analysis, extended X-ray absorption fine structure (EXAFS), multinuclear solid state nuclear magnetic resonance (NMR) spectroscopy, optical microscopy, differential scanning calorimetry (DSC), nanoindentation and gas sorption analysis are used to investigate the relationship between four crystalline MOF structures and the properties of the related glasses. Importantly, we show that the melting temperature (T_m) of a MOF can be lowered by altering the chemistry of the crystalline state, and we use ^{13}C and ^{15}N NMR to shed light on the mechanism of melting. Furthermore, we identify differences between these glasses, and amorphous (non MQG) phases formed upon heating the crystalline structures below T_m . Whilst some display glass-like behavior, others do not and appear more closely associated with the solvent collapse of first generation MOFs.²³

The MOF-glasses formed upon heating above T_m and cooling maintain the extended framework connectivity reminiscent of the crystalline MOF state, though in a highly long-range disordered array. Variations in crystal chemistries lead to large differences in T_m , glass transition temperatures (T_g) and fragilities (m), alongside the elastic modulus (E) and hardness (H) of the glasses formed by quenching. By identifying common features in those MOFs that undergo melting and vitrification, we suggest new opportunities for the family, which move away from the utilization of high surface areas.

Results and Discussion

Materials Selection

An inter-related set of MOFs was chosen to separate the effects of chemistry and topology upon glass formation. ZIF-4 crystallizes in the orthorhombic space group *Pbca*, possessing a *cag* topology, which is identical to the mineral variscite CaGa_2O_4 , and includes 8 nanopores per cell connected by apertures of diameter 2.1 Å (Fig. 1a).¹⁰ The structure is polymorphic with $\text{Zn}(\text{Im})_2$ (GIS), a more open framework (porosity, $P = 56.9\%$ compared to 23.6 % for ZIF-4, Table 1) which adopts a different, gismondine network topology (Fig. 1b) and crystallizes in space group *I4₁/a*.¹¹ The structure is not named in the literature. Mixed-ligand variants of ZIF-4 can be prepared using 5-methylbenzimidazole (*mbIm* – $\text{C}_8\text{H}_7\text{N}_2^-$) or benzimidazole (*bIm* – $\text{C}_7\text{H}_5\text{N}_2^-$), leading to compounds TIF-4 [$\text{Zn}(\text{Im})_{1.5}(\text{mbIm})_{0.5}$] and ZIF-62 [$\text{Zn}(\text{Im})_{1.75}(\text{bIm})_{0.25}$], which both adopt the same framework architecture and space group as ZIF-4 (Figs. 1c, d, S1).^{24,25}

Glass Transition and Melting Temperatures

In accordance with previous work, heating an evacuated sample of ZIF-4 results in structural collapse to an amorphous phase (termed $a\tau\text{ZIF-4}$) at 600 K, before recrystallization to a dense framework, ZIF-zni, just prior to melting at 863 K (Fig. 1e, Fig. 2a).¹⁶

The $\text{Zn}(\text{Im})_2$ (GIS) polymorph melts at an almost identical temperature to ZIF-4, after solvent loss in two stages at 400 K and 475 K (Fig. 2b). Upon heating in the DSC, TIF-4 undergoes solvent loss at a higher temperature of 525 K, before melting at 740 K (Fig. 2c). A partially evacuated sample of ZIF-62 (preheated at 440 K for 18 hours, Fig. S2), underwent the last stages of complete desolvation at 610 K (Fig. 2d), before melting at 710 K (i.e. 30K below TIF-4 and 150 K below ZIF-4).

The melting points are all clearly identified since the decomposition temperatures (T_d), in argon here are around 875 K (Fig. S2a). However, the T_d of ZIFs is atmosphere dependent,²⁶ and in air are *ca.* 673 K and 713 K for TIF-4 and ZIF-62 respectively, thus precluding the melting process (Fig. S3).

The decrease in melting point also provides insight into the mechanism. We previously inferred a reconstructive process upon melting and vitrification,¹⁹ involving Zn-N bond breaking and refor-

mation. This mechanism, based on the network topologies before and after melt-quenching and the relative weakness of the Zn-N bond within ZIF structures,²⁷ would be somewhat analogous to the description given by Kitagawa *et al.* of the melting in 1D zinc phosphate-imidazolate coordination polymers.²⁸ NMR data presented below provides supporting evidence in the observation of partially uncoordinated Im-based species in the recovered glasses.

Electron donating groups attached to the imidazolate ring would be predicted to strengthen the Zn-N bond, given the ‘soft-soft’ covalent interactions between the Zn^{2+} ion and Im-based ligands.²⁹ Indeed the NMR data presented later in this work support this hypothesis, in terms of the increased electron density present on the nitrogen atoms in bIm and mbIm. However, here the addition of an electron donating benzene ring to the imidazolate anion is accompanied by a *decrease* in melting point (Table 1). Unfortunately calculation of individual bond strengths was precluded by the transition from crystalline to solvent collapsed amorphous phase, prior to melting, in the cases of $\text{Zn}(\text{Im})_2$ (GIS), TIF-4 and ZIF-62.

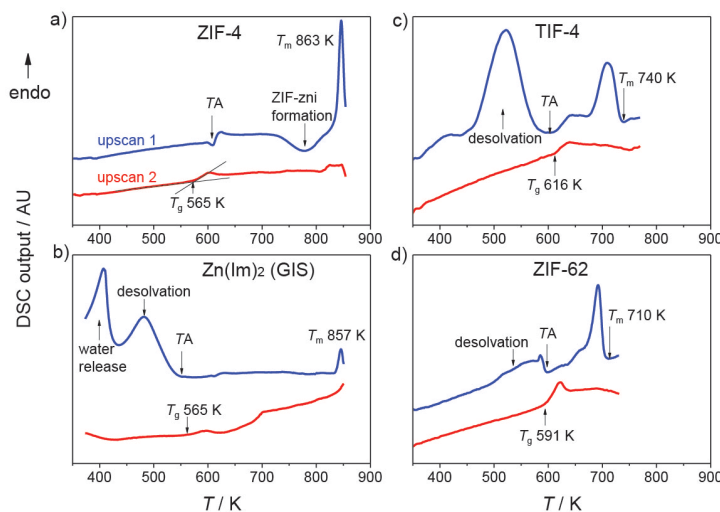
Previous work has shown that recrystallization of ZIF-4 to ZIF-zni involves an increase in mean N-Zn-N and Zn-Im-Zn angles, to closer to their ideal values (109.5° and 145°).³⁰ The inability of TIF-4 and ZIF-62 to support such changes (given the steric constraints placed upon the local coordination environment) may explain their lack of recrystallization to a dense phase prior to melting. This would be consistent with the higher melting temperature of ZIF-zni, compared to the amorphous phases of TIF-4 and ZIF-62 in which a distribution of values is expected. Some support is given to this latter statement by the greater distribution of N-Zn-N and Zn-Im-Zn angles, relative to ZIF-4 or ZIF-zni, in the amorphized sample of ZIF-4.³⁰

The liquids formed in-situ were cooled back to room temperature at 10 K / min, and glasses formed referred to as $a_g\text{ZIF-4}$, $a_g\text{Zn}(\text{Im})_2$ (GIS), $a_g\text{TIF-4}$ and $a_g\text{ZIF-62}$. A second DSC heating scan was then performed for all samples, which identified glass transition temperatures in each case (Fig. 2a-d, Table 1).

The glass transition temperature was observed to increase upon addition of successively larger ligands to the MOF structures, from 565 K, in the case of $a_g\text{ZIF-4}$ and $a_g\text{Zn}(\text{Im})_2$ (GIS), to 591 K and 606 K for $a_g\text{ZIF-62}$ and $a_g\text{TIF-4}$ respectively. The increase in T_g witnessed here for the series of topologically identical MOFs is consistent with observations in many organic polymers,³¹ where addition of bulky side groups is related to restriction of backbone motion and flexibility upon cooling of the liquid phase toward T_g .

Solvent Collapse and ‘Glass-like’ Behavior

Variable temperature X-ray diffraction was used to probe the relationship between solvent removal and structural collapse (amorphization) in the samples. Successful solvent removal from the crystalline ZIF-4 structure has been reported previously, before a



separate amorphization event. This amorphous structure, named $a_T\text{ZIF-4}$, has been observed to possess a glass transition feature upon quenching and reheating.¹⁹

In contrast, solvent removal from $\text{Zn}(\text{Im})_2$ (GIS) is associated with framework collapse (Fig. S4), and

formation of an X-ray amorphous material termed $a_T\text{Zn}(\text{Im})_2$ (GIS). This is consistent with the collapse of ZIF-6, a closely related framework, upon solvent removal.³² Upon cooling to room temperature and reheating, $a_T\text{Zn}(\text{Im})_2$ (GIS) displays a glass-transition (Fig. S5), though unlike $a_T\text{ZIF-4}$, no recrystallization is observed before melting at 857 K. Solvent release from TIF-4 also causes structural collapse, and formation of an X-ray amorphous phase (Fig. S4) termed $a_T\text{TIF-4}$ at 650 K (i.e. after the first solvent release endotherm). $a_T\text{TIF-4}$ was recovered to room temperature, and, dissimilar to the glass-like $a_T\text{ZIF-4}$ or $a_T\text{Zn}(\text{Im})_2$ (GIS), did not show any T_g -like features upon rescanning in the DSC (Fig. S6a).

Investigation into $a_T\text{ZIF-62}$ also failed to find any glass-like behavior (Fig. S6b), providing clear evidence for differences in amorphous (non melt-quenched) and MQG phases. This sequence of phase transitions helps explain the relative sharpness of the observed DSC melting peaks. The peak is relatively sharp in the heating scan of ZIF-4 (i.e. the melting of ZIF-zni), which implies that the crystals are uniform.

Figure 2: Enthalpic responses of the four samples on both the first (blue) and second (red) DSC heating upscans at 10 K/min. Thermal amorphization (T_A), water release, desolvation, crystallization, melting temperature (T_m) and glass transition temperature (T_g) are indicated. a) ZIF-4 [$Zn(Im)_2$], b) ZIF-GIS [$Zn(Im)_2$], c) TIF-4 [$Zn(Im)_{1.5}(mbIm)_{0.5}$] and d) ZIF-62 [$Zn(Im)_{1.75}(bIm)_{0.25}$]. T_m refers to the offset temperature of the melting peak, whereas T_g is the onset temperature of glass transition peak. Initial endotherms related to solvent loss are not witnessed in the case of ZIF-4 due to prior structural evacuation. ZIF-62 was subjected to annealing at 440 K for 18 hours prior to the DSC scanning, resulting in a smaller solvent release endotherm, associated with a mass loss of 0.55 % (Fig. S2).

The peak obtained due to melting of ZIF-GIS is however slightly broader, though it also appears smaller in intensity due to the far larger desolvation enthalpies recognized from this more porous system. The melting peaks observed upon the heating scans of TIF-4 and ZIF-62 are broader still, though this is ascribed to melting of the amorphous (non MQG) phases, and reflects some degree of structural heterogeneity.

Fragility Measurements

The fictive temperature, T_f , of a glass (i.e. in the non-liquid state) may be thought of as the temperature at which the structure of an equilibrium liquid is frozen in.³³ The dependence of T_f upon the heating rate used in the DSC scan (q_h) (Fig. S5), allows determination of the kinetic fragility index, m ,^{19,33,34} which quantifies the speed of the dynamical processes of a liquid as it approaches the glass transition temperature. Interestingly, despite ZIF-4 and $Zn(Im)_2$ (GIS) possessing the same chemical formula and melting at the same temperature, the liquids produced exhibit very different fragilities ($m = 39$ and 17 respectively, Fig. 3). The differences here were confirmed by evaluation of m for $a_7Zn(Im)_2$ (GIS) ($m = 15$), which lies close to that of $a_9Zn(Im)_2$ (GIS) (Fig. S7). This is consistent with the noticeably similar fragilities of a_9ZIF-4 ($m = 39$) and a_7ZIF-4 ($m = 41$).

The different fragilities of the liquids formed upon melting of ZIF-4 and $Zn(Im)_2$ (GIS) may stem from a remnant influence of the network architecture of the solid phase, given the relatively small window between melting and quenching of the samples. Indeed, whilst chemically identical, the phases immediately prior to melting are not the same (ZIF-zni and $a_7Zn(Im)_2$ (GIS) respectively). Fragility was also observed to decrease on going from ZIF-4 ($m = 39$) to ZIF-62 ($m = 35$) and then to TIF-4 ($m = 23$), and hence, for those frameworks displaying the *cag* topology, fragility decreases with increasing linker content and size.

Whilst an increase in fragility with increasing linker size may have been expected based on free volume considerations and the increase in T_g , similar changes in the fragility index of other glass-forming polymers have been noted,^{31,35} and ascribed to the relative side group stiffness compared to the polymer backbone. The lower kinetic fragilities of the $Zn(Im)_2$ (GIS) and TIF-4 melts compared to the ZIF-4 melt are consistent with smaller C_p increases during the glass transition, given that the latter is a measure of thermodynamic fragility.²⁰

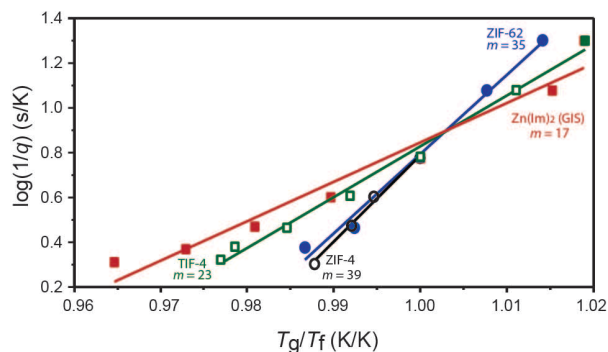


Figure 3. Fragilities of ZIF-4, $Zn(Im)_2$ (GIS), TIF-4 and ZIF-62, determined from the dependence of fictive temperature (T_f) on the heating rate (q_h) by using the DSC method. Large values of m may indicate fragile liquids that form relatively ductile glasses (e.g. toluene, $m = 105$), whilst lower fragilities have been suggested to characterize 'strong' liquids, that vitrify to yield brittle glasses (e.g. silica, $m = 20$).³⁶⁻³⁸ Black open circles: ZIF-4, Red squares: $Zn(Im)_2$ (GIS), Green open squares: TIF-4, Blue closed circles: ZIF-62.

Pair Distribution Function and X-ray Absorption Fine Structure Measurements

Bulk samples of each crystalline phase were subsequently heated in a tube furnace under flowing argon to 863 K (ZIF-4), 857 K ($Zn(Im)_2$ (GIS)), 740 K (TIF-4) and 710 K (ZIF-62), i.e. above the respective melting endotherms but before thermal decomposition. Cooling of the samples under argon yielded X-ray amorphous products (Fig. S1), with vitrification resulting in remarkable morphological changes (Fig. 4). All single crystals show appreciable flow during vitrification, whilst the needle structures of $Zn(Im)_2$ (GIS) undergo macroscopic changes into sheet-like glasses of $a_9Zn(Im)_2$ (GIS). Micrographs of these glasses under parallel and crossed-polarized light are reported in Fig. S8, confirming optical isotropy.

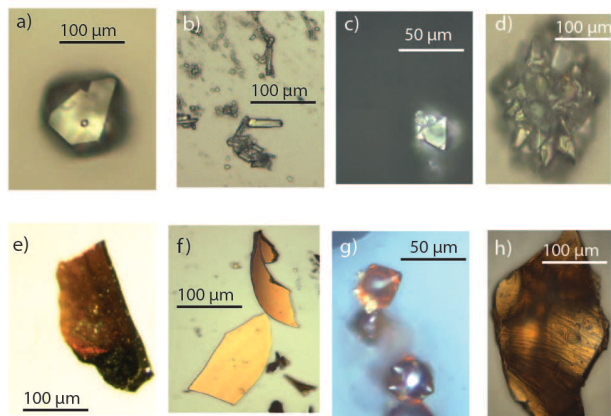


Figure 4: Optical images of crystalline samples of ZIF-4, $\text{Zn}(\text{Im})_2$ (GIS), TIF-4 and ZIF-62 (a-d). Clearly, the products formed upon melting and quenching (e-h) resemble glasses formed from macroscopic flow.

Elemental analysis revealed few differences between crystalline and vitrified phases, aside from those associated with the loss of solvent (SI-4), whilst they demonstrated no uptake of N_2 gas during sorption measurements (Table S1). Ultra-violet visible (UV-VIS) spectroscopy performed on the crystalline samples showed the expected bathochromic shift in the position of λ_{max} from those samples incorporating the Im linker (ZIF-4 and $\text{Zn}(\text{Im})_2$ (GIS)), to those with bIm and mbIm organics (TIF-4 and ZIF-62). In the latter two cases, absorption bands were also much broader. On vitrification, few distinguishable absorption bands were recorded (Fig. S9). Curiously, whilst Raman spectroscopy also demonstrated similarities between crystalline phases (Fig. S10) and yielded little information on $a_g\text{ZIF-4}$, $a_g\text{Zn}(\text{Im})_2$ (GIS) or $a_g\text{TIF-4}$ due to their non-transparent nature, the spectrum of $a_g\text{ZIF-62}$ contained features extremely similar to the crystalline framework.

Diffuse reflectance infrared spectroscopy (DRIFTS) was also performed on the samples (Fig. S11). In all cases, spectra of the crystalline MOF and its corresponding glass were largely similar, though are dominated by contributions from the imidazole-based rings. Merging of bands associated with stretching of the aromatic organic rings was observed in the glass phases.

EXAFS was performed on both crystalline and vitrified samples in order to provide information on the first zinc coordination shell, and to determine whether the tetrahedral configuration was maintained in the glass phase. Data extracted through Fourier transformation of the X-ray absorption spectra are similar between crystal and corresponding glasses (Fig. 5). In particular, all spectra exhibit one strong peak at *ca.* 1.6 Å. Comparison with other EXAFS data on ZIFs, which were also not phase shift corrected, confirm this feature corresponds to the zinc-nitrogen distance at 2 Å.³⁹ This peak is invariant in both position and intensity upon vitrification, and confirms the local environment of Zn^{2+} ions is identical in the glasses (i.e. each is coordinated by four nitrogen atoms in a tetrahedral environment). Further similarities between crystal and glass to 4 Å are expected given this limit represents the distance to the second N donor atom on the rigid, planar imidazolate ligand.

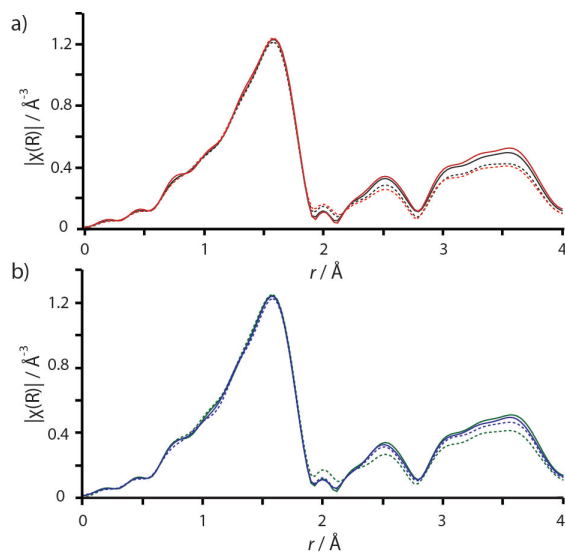


Figure 5: 'Pseudo' radial distribution functions for crystalline (solid lines) and vitrified (broken lines) samples of (a) ZIF-4 and $\text{Zn}(\text{Im})_2$ (GIS) and (b) TIF-4 and ZIF-62. Data were extracted through Fourier transformation of the X-ray absorption spectra (Fig. S12), themselves obtained at the K edge of zinc. Phase shift corrections were not applied. Black – ZIF-4, red – $\text{Zn}(\text{Im})_2$ (GIS), green – TIF-4 and blue – ZIF-62.

Given recent advances in the study of disordered MOFs by PDF methods,⁴⁰⁻⁴² the detailed chemical structures of all samples here were probed by collecting room temperature X-ray total scattering data (Ag source, $\lambda = 0.561 \text{ Å}$, $Q_{\text{max}} = 20 \text{ Å}^{-1}$). The resultant, near identical structure factors $S(Q)$ (Fig. S13) of the vitrified materials confirm their amorphous nature. Subsequent Fourier Transform yields the PDFs, $D(r)$, though modeling was not attempted due to insufficient data quality.

Whilst the crystalline sample PDFs contain long range oscillations attributed to their crystallographic order on length scales exceeding 20 Å (Fig. 6a), those of the glasses are essentially featureless above 8 Å (Fig. 6b). Below this distance, all eight PDF traces are virtually identical, with only small differences in peak intensities. They also display a remarkable similarity to those of ZIFs amorphized by ball-milling and at lower temperatures (prior to recrystallization and melting).⁴³ Assignment of the five physical sharp features below 6 Å (the first peak at 0.74 Å is considered an artifact as it is typically very difficult to obtain reliable data below $\sim 1 \text{ Å}$ from lab-based X-ray total scattering instruments) was performed by using the PDFGUI software to calculate the partial PDFs for the constituent atom-pairs of ZIF-4 (Fig. S14).^{10,44}

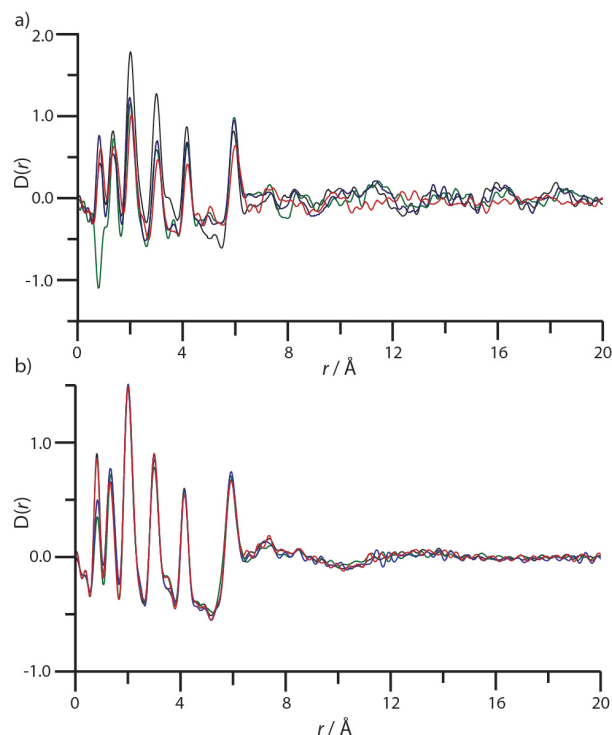


Figure 6: (a) Pair distribution function $D(r)$ calculated via Fourier Transform of the X-ray total scattering function $S(Q)$, for ZIF-4 (black), Zn(Im)_2 (GIS) (red), TIF-4 (green), ZIF-62 (blue). (b) Pair distribution function $D(r)$ calculated via Fourier Transform of the X-ray total scattering function $S(Q)$, for $a_g\text{ZIF-4}$ (black), $a_g\text{Zn(Im)}_2$ (GIS) (red), $a_g\text{TIF-4}$ (green), $a_g\text{ZIF-62}$ (blue).

The first real feature at 1.3 Å corresponds to C-C or C-N aromatic linkages within the imidazolate ring, whilst the more intense peak at 2 Å indicates nearest neighbor Zn and N atoms – importantly confirming the retention of metal-organic association in the glass phases. Zn-N distances also account for the peak at 4.1 Å, though this is the distance between metal centres and the second N atom in the organic ligand. These two features are separated by a peak at 3 Å, due to correlations between nearest neighbor Zn and C atoms.

At longer distances, all PDFs are dominated by scattering from Zn due to its larger scattering cross section relative to those of C, N and H. The last intense peak in the spectra of the glasses occurs at 6 Å and belongs to nearest zinc atom neighbors. This limit of short range order is consistent with prior reports of amorphous ZIFs and the retention of metal-organic-metal connectivity.⁴³ This is consistent with PDF studies of silica glass,⁴⁵ where the local tetrahedral coordination and order around Si centres is preserved to 3.1 Å, though framework order is lost. The longer distance associated with this local order in ZIFs is due to the larger bridging ligand ($\text{C}_3\text{H}_3\text{N}_2$ compared to O). The similarities of the PDFs of crystalline TIF-4 and ZIF-62, to that of ZIF-4, is due to the negligible effect on the PDFs of additional contributions from the extra aromatic carbon atoms of the benzene rings in the structures of TIF-4 and ZIF-62.

A smaller, slightly broader peak centered at 7 Å is visible in the PDFs of the glasses. This distance is populated by Zn-C and Zn-N correlations in the partial PDFs of ZIF-4, where both non-metal atoms are located on the second-nearest imidazolate ion to the metal center. It is possible, though not confirmed, that this small feature suggests a Zn-Im-Zn-Im motif is present in all glasses, and

provides possible evidence of order extending beyond Zn-Im-Zn correlations.

Solid State Nuclear Magnetic Resonance Data

The ^{13}C cross polarization (CP) magic angle spinning (MAS) solid state ^{13}C and ^{15}N NMR spectra of the crystalline samples show most of the individual carbon and nitrogen atoms in the asymmetric unit cell (Fig. 7a). Differences in the ^{13}C and ^{15}N spectra of crystalline ZIF-4⁴⁶ and Zn(Im)_2 (GIS) are reflective of the different number of crystallographically independent ligands (4 cf. 16), whilst additional resonances at 162.1, 42–12 ppm (in the ^{13}C NMR) and 133 ppm (in the ^{15}N NMR) and correspond to diethylformamide inside the pores of Zn(Im)_2 (GIS) (SI-9).

Additional ^{13}C resonances in the spectra of TIF-4 and ZIF-62 correspond to mbIm or bIm ligands (see Table S3 for complete assignments). Notably, the presence of these linkers was also confirmed by two additional resonances in the ^{15}N spectra of TIF-4 and ZIF-62, the smaller shift observed for the bIm/mbIm ligands (190.2/188.8 ppm) vs the Im ligands (205.2 ppm) reflecting the slightly larger shielding effect of the benzimidazolate group.⁴⁷

All individual resonances in the ^{13}C and ^{15}N CP MAS NMR spectra of $a_g\text{ZIF-4}$, $a_g\text{Zn(Im)}_2$ (GIS), $a_g\text{TIF-4}$ and $a_g\text{ZIF-62}$ glasses (Fig. 7b) are much broader than for the corresponding crystalline materials and this is consistent with the existence of amorphous phases, as noted previously.⁴⁶ Importantly, the NMR results of these materials confirm that the organic linkers remain intact in the vitrified products, as previously observed in other amorphous ZIFs prepared by mechanosynthesis⁴⁶ (see Table S4 for spectral assignments). The solvent signals observed in the crystalline phases have disappeared, in agreement with the solvent removal observed by DSC.

Both ^{13}C and ^{15}N NMR spectra of $a_g\text{ZIF-4}$ and $a_g\text{Zn(Im)}_2$ (GIS) are virtually identical with the NCN and NCC carbons and CNC nitrogens of the Im ligand appearing at the same chemical shift (Table S4). Two additional small resonances are also observed and are assigned to uncoordinated imidazole based on known chemical shifts.⁴⁶ Such differences between crystal and glasses were not identifiable in the PDF measurements. Similar partial de-coordination of 2-methylimidazole was previously observed in amorphous ZIF-8 (prepared by ball-milling) but not in other unsubstituted imidazole as in amorphous ZIF-4 and ZIF-zni,⁴⁶ suggesting that melt-quenching is a more energy rich process than milling.

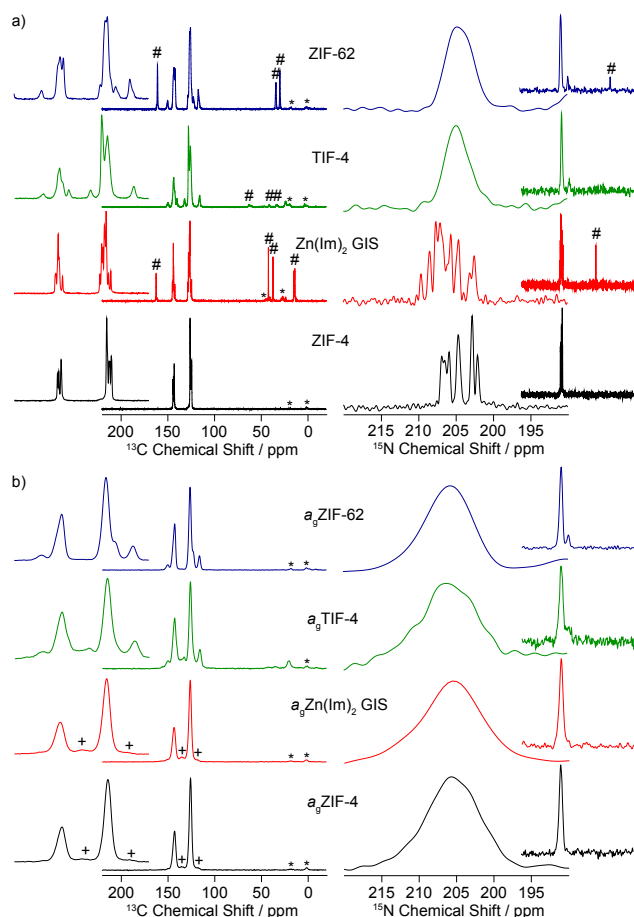


Figure 7: ^{13}C (left) and ^{15}N (right) CP MAS NMR spectra of (a) ZIF-4 (black), $\text{Zn}(\text{Im})_2$ (GIS) (red), TIF-4 (green), ZIF-62 (blue), (b) and the corresponding glass phases a_{g} ZIF-4, a_{g} $\text{Zn}(\text{Im})_2$ (GIS), a_{g} TIF-4, a_{g} ZIF-62, obtained at 9.4 T. Spinning sidebands are marked with asterisks (*), de-coordinated Im ligands by plus (+) and adsorbed residual solvent synthesis by dash (#). ^{13}C inserts show magnified views of the 160–110 ppm region, while ^{15}N insert shows a wider 290–50 ppm view. Proposed spectral assignments are given in Tables S3–S4.

Although at first sight the NMR data obtained on the mixed-ligand glasses a_{g} TIF-4 and a_{g} ZIF-62 appear relatively similar with the observation of the Im ligands (at 142 and 126 ppm for NCN and NCC carbons, and at 206 for CNC nitrogen) and the benzimidazole moieties (at 145–149 and 116 ppm for the NCN and CHCN, and at 190 ppm for CNC), close inspection in the ^{13}C spectra reveals differences and the identification of both the mbIm linker in a_{g} TIF-4 and the bIm moieties in a_{g} ZIF-62. Specifically, the ^{13}C NMR fingerprints of mbIm are clearly seen in Fig. 7b with the observation of the CHCHCN (140 ppm), CCH₃CHCN (132 ppm) and CH₃ carbons (21 ppm), the bIm ligand gives rise to a signal at 123 ppm typical of the CHCHCN carbon. We note that in spite of the fact that we could not detect free imidazole or (5-methyl)benzimidazole due to their overlapping resonances with the ones of a_{g} TIF-4 and a_{g} ZIF-62, it is likely that some ligand de-coordination process also occurs.

Mechanical Properties and Densities

The densities of the crystalline materials, the amorphous (non MQG) phases and the melt-quenched glasses themselves, were

probed using gas pycnometry. The densities of the dense ZIF-zni phase (for ZIF-4) and the amorphous phases formed prior to melting (for $\text{Zn}(\text{Im})_2$ (GIS), TIF-4 and ZIF-62) were all higher than the initial crystalline frameworks (Table S2). This is unsurprising, given the collapse of other porous crystals such as ZrW_2O_8 and silicalite.^{48,49} Density changes from these phases to the melt quenched glasses were much less significant, though still involved an increase. The sample with the lowest T_{m} , ZIF-62, gave rise to the least dense glass in the study, though curiously an increase in density of the glass formed by quenching the liquid from 845 K (cf just above T_{m}) was observed.

The mechanical properties of TIF-4, along with those of a_{g} ZIF-4, a_{g} $\text{Zn}(\text{Im})_2$ (GIS), a_{g} TIF-4 and a_{g} ZIF-62, were probed by nanoindentation on suitable single crystals or monoliths. E , the elastic modulus, measures the ease of deformation along one axis of a material and, as such, has been used as a measure of MOF ‘stiffness’. Hardness, H , indicates the resistance to plastic deformation of a material, though it is heavily dependent upon experimental parameters.⁵⁰ Values of E and H are included in Table S5.

Analysis of the load-displacement data (Fig. S15) revealed the anisotropic elastic modulus of TIF-4 ($E_{111} \sim 6.4$ GPa) to be significantly greater than the corresponding value for ZIF-4 ($E_{111} \sim 4.7$ GPa) reported in a previous study,¹⁶ which is consistent with the higher density of TIF-4, and may be ascribed to the larger organic present. Upon vitrification to a_{g} TIF-4, significant stiffening is observed ($E \sim 7.9$ GPa), which reflects an increase in pycnometric density. Indeed, the elastic moduli of the glasses correlate well with their pycnometric densities (Fig. 8), whilst those of identical chemical composition possess comparative elastic moduli.

The large temperature range between T_{m} and T_{d} in ZIF-62 allowed heating to 845 K (i.e. 135 K above T_{m}), without framework decomposition. This sample was vitrified upon cooling, and found to exhibit a significantly larger elastic modulus compared to the sample cooled from just above T_{m} , ($E \sim 8.8$ GPa, Fig. S15). This increase in rigidity is expected, given similar density of the sample compared to others in the study, and suggests a better structural equilibration of the glass formed from higher temperature melt, despite the identical cooling rates used. In analogous fashion, a *ca.* 33% increase in hardness was also noted. Interestingly however, H was invariant between TIF-4 and a_{g} TIF-4 (Fig. S16). All H values were observed to lie in the range 0.2 – 1.5 GPa, which is in agreement with previously determined H values for MOFs.

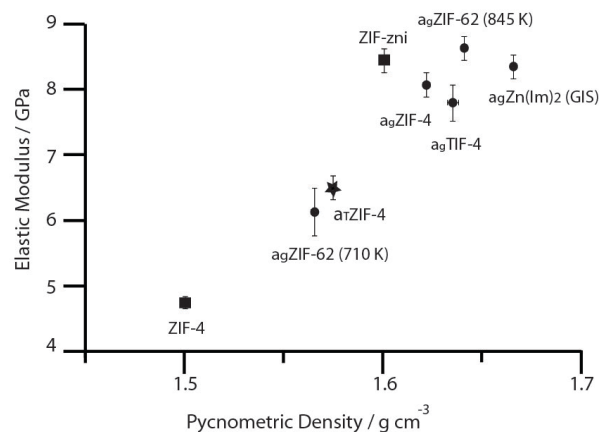


Figure 8: Correlation between elastic modulus and physical density of the melt quenched glasses, temperature amorphized ZIF-4 and the crystalline ZIF-4 and ZIF-zni.

Conclusion

The melting point of a metal-organic framework was manipulated by altering the chemical composition of the crystalline framework, prior to melting. This approach, in which T_m can be lowered by the addition of varying quantities of larger organic ligands, provides routes to achieve generalization of the phenomenon and achieving melting in MOFs which do not obey the current necessary $T_m < T_d$ condition. The mechanism involves partial linker decoordination, and thus the melting temperature is expected to be partially dependent upon the metal-ligand bond strength. Sterically bulky species are observed to decrease the melting point, whilst structural anisotropy allows melting, instead of thermal decomposition (i.e. simultaneous de-coordination of all metal-ligand bonds).

Alongside reducing T_m , the introduction of successively larger organic ligands into topologically identical frameworks decreases the fragilities of the glass forming liquids. The effect of framework architecture upon melting temperature however appears less clear, with identical values of T_m reported across chemically identical, topologically distinct systems. In this latter case, the fragility index is however very different, which may suggest a topological contribution to the melting process.

The effect of increasing the size of organic ligand upon elastic moduli of the glasses formed can also be predicted. Rationalized in terms of packing ability, the decrease in elastic moduli upon increasing the size of the organic component presented here is reminiscent of work on hybrid organic-inorganic sol gels,⁵¹ and points toward significant analogies between these materials and MOF-glasses. The striking result of an increase in E upon quenching of the liquid formed from heating ZIF-62 above T_m merits further investigation.

The demonstration of the melting of several three-dimensional MOFs has important consequences for the growing list of potential applications for this burgeoning class of materials. First and foremost, melting opens up new routes to hybrid glasses, the chemical functionality of which may be altered by utilizing the chemical versatility of the crystalline MOF state. Through this work, we expect that the family of MOF glasses, i.e. a new type of MQG, can be expanded for various applications (e.g. in advanced photonics and lighting). Alongside the glasses themselves, *in-situ* formation from liquids will prove of great interest in producing precise, desired morphologies via melt-casting or melt-spinning processes. However, this new area of MOF research leads to questions such as the nature of the liquids produced,⁵² the effect of quenching rate upon mechanical properties, and the predictability of the phenomenon.

Experimental Section

Synthesis. Microcrystalline powders of the four crystalline MOFs were synthesised using established methodology (Figs. S1, S2).^{11,24,25,53}

Differential scanning calorimetry (DSC). DSC experiments were performed using a Netzsch STA 449 F1 instrument in an inert argon atmosphere. The samples were placed in a platinum crucible situated on a sample holder of the DSC at room temperature and subjected to varying numbers of up- and downscans, depending on

the purpose of the measurements. After natural cooling to room temperature, the subsequent up-scans were performed using the same procedure as for the first. Using DSC we determined the fictive temperature as a function of the up and down scan rate. Based on the heating rate dependence of fictive temperature liquid fragility indices were evaluated according to previous literature.¹⁹

Gas pycnometry and N₂ sorption. Pycnometric measurements were performed using a Micromeritics Accupyc 1340 helium pycnometer. The typical mass used was 200 mg, the values quoted being the mean and standard deviation from a cycle of 10 measurements. N₂ sorption isotherm measurements were performed on a Micromeritics Tristar II 3020 (Micromeritics, Norcross, GA) at 77K. Between 80 and 100 mg of material was used for each measurement. Surface areas were estimated by applying the Brunauer–Emmett–Teller (BET) equation.

X-ray Diffraction. Room temperature PXRD data ($2\theta = 5\text{--}30^\circ$) were collected with a Bruker-AXS D8 diffractometer using Cu K α ($\lambda = 1.540598 \text{ \AA}$) radiation and a LynxEye position sensitive detector in Bragg-Brentano para-focusing geometry. Variable temperature PXRD data were collected in Bragg-Brentano geometry with a Bruker-AXS D8 diffractometer equipped with primary Gobel mirrors for parallel Cu K α X-rays, a Vantec position sensitive detector and an MRI heating stage. Collections conditions were: $3\text{--}30^\circ$ in 2θ , 0.02 step size, 100 seconds/step, divergence slit 0.6 mm. X-ray total scattering data were collected at room temperature on the crystalline and a_m -ZIFs using a PANalytical Ag-source X'pert Pro MPD lab diffractometer ($\lambda = 0.561 \text{ \AA}$). Data collection was performed using loaded 1.0 mm diameter quartz capillaries and collection times of approximately 18 hrs. Corrections for background, multiple scattering, container scattering and absorption were applied using the GudrunX program.⁵⁴⁻⁵⁶

Nanoindentation. The Young's modulus (E) of the samples was measured using an MTS Nanoindenter XP at ambient conditions. The Miller indices of single crystals of TIF-4 were predicted using the Mercury software.⁵⁷ Samples were mounted in an epoxy resin and polished using increasingly fine diamond suspensions. Indentation experiments were performed under the dynamic displacement controlled mode, at a constant strain rate of 0.05 s^{-1} . All tests were conducted using a three-sided pyramidal (Berkovich) diamond indenter tip, to a maximum surface penetration depth of 500 nm. The load-displacement data collected were analysed using the Oliver & Pharr method.⁵⁸ A Poisson's ratio of 0.2 was used, in accordance with prior studies on ZIF materials.¹²

Raman Spectroscopy. The Raman spectra were measured with a LabRAM HR Evolution HORIBA Scientific instrument equipped with an Olympus 100x microscope objective. The measurements were performed at room temperature in the range $100 - 4000 \text{ cm}^{-1}$ with 10 accumulation scans and 2 s acquisition time.

Diffuse Reflectance Infrared and UV-Visible Spectroscopy. Diffuse reflectance infrared spectra (DRIFTS) were recorded on a Nicolet 7600 FTIR spectrometer equipped with an MCT detector. The spectra were collected in a KBr mixture under N₂ purge using KBr as the background. UV-Vis diffuse-reflectance spectra were collected at room temperature using a Shimadzu UV-3600 PC double-beam, double-monochromator spectrophotometer operating from 200 to 800 nm. BaSO₄ was used as a non-absorbing reflectance reference.

Polarized Light Microscopy. All materials were studied with a Zeiss Axioplan and Canon A630 polarized light petrographic photomicroscope.

Extended X-ray Absorption Fine Structure Spectroscopy. X-ray absorption spectra were collected in transmission mode on Beamline B18 at the Diamond light source (DLS), operating in a 10 min top-up mode for a ring current of 200 mA and an energy of 3 GeV. The radiation was monochromated with a Si(111) double crystal, and harmonic rejection was achieved through the use of two platinum-coated mirrors operating at an incidence angle of 6.0 mrad. The monochromator was calibrated using the K-edge of a Zn foil, taking the first inflection point in the Zn edge as 9659 eV. Three scans of each sample were taken, aligned using data taken on Zn foil reference, and subsequently averaged. The Athena software program was used for data processing. Data in the range $3 < k < 15 \text{ \AA}^{-1}$ were Fourier Transformed and k^2 weighted. Phase shift corrections were not applied.

Solid state NMR spectroscopy. All solid-state NMR measurements were performed on a 9.4 T Bruker Avance III HD NMR spectrometer equipped with a 4 mm HXY triple resonance MAS probe at ^1H Larmor frequency of 400.13 MHz with the X and Y channels tuned to ^{13}C and ^{15}N at 100.63 and 40.55 MHz, respectively. All NMR spectra were obtained with CP at MAS frequencies of 12.5 kHz and 10 kHz for ^{13}C and ^{15}N , respectively. ^1H pulses and SPINAL-64 heteronuclear decoupling⁵⁹ were performed at a radio-frequency (rf) field amplitude of 83 kHz. ^{13}C CP MAS experiments were obtained with optimized contact times of 2 ms and with a ^{13}C rf field of 40 kHz, while the ^1H rf field amplitude was ramped to obtain maximum signal at a ^1H rf field of approximately 60 kHz. ^{15}N CP MAS experiments were obtained with contact times of 5 ms and with a ^{15}N rf field of 33 kHz, while the ^1H rf field amplitude was ramped to obtain maximum signal at a ^1H rf field of approximately 40 kHz. ^{13}C and ^{15}N chemical shifts (± 0.2 and ± 1 ppm for the crystalline and glasses materials, respectively) were externally referenced to the CH_3 group of alanine at 20.5 ppm (corresponding to the CH_2 group of adamantane at 29.45 ppm)⁶⁰ and the NH_3^+ group of glycine at 33.4 ppm (corresponding to liquid NH_3 at 0 ppm).⁶¹ All samples were packed in air.

ASSOCIATED CONTENT

Supporting Information. PXRD, TGA, DSC, elemental analysis, gas sorption, EXAFS, total scattering, full NMR spectral assignments and nanoindentation data. This material is available free of charge via the Internet at <http://pubs.acs.org>.

AUTHOR INFORMATION

Corresponding Author

*tdb35@cam.ac.uk

Notes

The authors declare no competing financial interest.

ACKNOWLEDGMENTS

TDB would like to thank Trinity Hall (University of Cambridge) for funding. We thank Diamond Light Source for access to beamline B18 (SP14249-1) that contributed to the results presented here. We thank Dr. Giannantonio Cibin and Dr. Stephen Parry for their assistance with the EXAFS measurements. FB thanks EPSRC (grant EP/M00869X/1) and the University of Liverpool for funding. OKF gratefully acknowledges funding from the Army Research Office (project number

W911NF-13-1-0229). SATR is grateful for funding from the Natural Environment Research Council.

REFERENCES

- (1) Furukawa, H.; Cordova, K. E.; O'Keeffe, M.; Yaghi, O. M. *Science* **2013**, *341*, 974.
- (2) Nugent, P.; Belmabkhout, Y.; Burd, S. D.; Cairns, A. J.; Luebke, R.; Forrest, K.; Pham, T.; Ma, S. Q.; Space, B.; Wojtas, L.; Eddaoudi, M.; Zaworotko, M. J. *Nature* **2013**, *495*, 80.
- (3) Shimizu, G. K. H.; Taylor, J.; Kim, S. *Science* **2013**, *341*, 354.
- (4) Jain, P.; Ramachandran, V.; Clark, R. J.; Zhou, H. D.; Toby, B. H.; Dalal, N. S.; Kroto, H. W.; Cheetham, A. K. *J. Am. Chem. Soc.* **2009**, *131*, 13625.
- (5) Stock, N.; Biswas, S. *Chem. Rev.* **2012**, *112*, 933.
- (6) Morris, R. E.; Cejka, J. *Nat Chem* **2015**, *7*, 381.
- (7) Allendorf, M. D.; Stavila, V. *CrystEngComm* **2015**, *17*, 229.
- (8) Guillerme, V.; Ragon, F.; Dan-Hardi, M.; Devic, T.; Vishnuvarthan, M.; Campo, B.; Vimont, A.; Clet, G.; Yang, Q.; Maurin, G.; Férey, G.; Vittadini, A.; Gross, S.; Serre, C. *Angew. Chem. Int. Ed.* **2012**, *51*, 9267.
- (9) McDonald, T. M.; Mason, J. A.; Kong, X. Q.; Bloch, E. D.; Gygi, D.; Dani, A.; Crocella, V.; Giordanino, F.; Odoh, S. O.; Drisdell, W. S.; Vlaisavljevich, B.; Dzubak, A. L.; Poloni, R.; Schnell, S. K.; Planas, N.; Lee, K.; Pascal, T.; Wan, L. W. F.; Prendergast, D.; Neaton, J. B.; Smit, B.; Kortright, J. B.; Gagliardi, L.; Bordiga, S.; Reimer, J. A.; Long, J. R. *Nature* **2015**, *519*, 303.
- (10) Park, K. S.; Ni, Z.; Cote, A. P.; Choi, J. Y.; Huang, R. D.; Uribe-Romo, F. J.; Chae, H. K.; O'Keeffe, M.; Yaghi, O. M. *Proc. Natl. Acad. Sci. U.S.A.* **2006**, *103*, 10186.
- (11) Tian, Y. Q.; Zhao, Y. M.; Chen, Z. X.; Zhang, G. N.; Weng, L. H.; Zhao, D. Y. *Chem.-Eur. J.* **2007**, *13*, 4146.
- (12) Tan, J. C.; Bennett, T. D.; Cheetham, A. K. *Proc. Natl. Acad. Sci. U.S.A.* **2010**, *107*, 9938.
- (13) Horike, S.; Shimomura, S.; Kitagawa, S. *Nat Chem* **2009**, *1*, 695.
- (14) Schneemann, A.; Bon, V.; Schwedler, I.; Senkovska, I.; Kaskel, S.; Fischer, R. A. *Chem. Soc. Rev.* **2014**, *43*, 6062.
- (15) James, S. L.; Friscic, T. *Chem. Soc. Rev.* **2013**, *42*, 7494.
- (16) Bennett, T. D.; Goodwin, A. L.; Dove, M. T.; Keen, D. A.; Tucker, M. G.; Barney, E. R.; Soper, A. K.; Bithell, E. G.; Tan, J. C.; Cheetham, A. K. *Phys. Rev. Lett.* **2010**, *104*, 115503.
- (17) Chen, W.; Horike, S.; Inukai, M.; Kitagawa, S. *Polym. J.* **2015**, *47*, 141.
- (18) Umeyama, D.; Horike, S.; Inukai, M.; Itakura, T.; Kitagawa, S. *J. Am. Chem. Soc.* **2015**, *137*, 864.
- (19) Bennett, T. D.; Tan, J. C.; Yue, Y. Z.; Baxter, E.; Ducati, C. D.; Terril, N.; Yeung, H. Y.; Zhou, Z.; Chen, W.; Henke, S.; Cheetham, A. K.; Greaves, G. N. *Nat Commun* **2015**, *6*, 8079.
- (20) Angell, C. A. *Science* **1995**, *267*, 1924.
- (21) Novak, B. M. *Adv. Mater.* **1993**, *5*, 422.
- (22) Vendamme, R.; Onoue, S. Y.; Nakao, A.; Kunitake, T. *Nat. Mater.* **2006**, *5*, 494.
- (23) Kitagawa, S.; Kondo, M. *Bull. Chem. Soc. Jpn.* **1998**, *71*, 1739.
- (24) Gustafsson, M.; Zou, X. D. *J. Porous Mat* **2013**, *20*, 55.
- (25) Wu, T.; Bu, X. H.; Zhang, J.; Feng, P. Y. *Chem. Mater.* **2008**, *20*, 7377.
- (26) Yin, H.; Kim, H.; Choi, J.; Yip, A. C. K. *Chem. Eng. J.* **2015**, *278*, 293.
- (27) Gadipelli, S.; Travis, W.; Zhou, W.; Guo, Z. *Energ Environ Sci* **2014**, *7*, 2232.

- (28) Horike, S.; Chen, W.; Itakura, T.; Inuaki, M.; Umeyama, D.; Asakura, H.; Kitagawa, S. *Chem. Commun.* **2014**, 50, 10241.
- (29) Boussouf, K.; Boulmene, R.; Prakash, M.; Komiha, N.; Taleb, M.; Al-Mogren, M. M.; Hochlaf, M. *Phys Chem Chem Phys* **2015**, 17, 14417.
- (30) Beake, E. O.; Dove, M. T.; Phillips, A. E.; Keen, D. A.; Tucker, M. G.; Goodwin, A. L.; Bennett, T. D.; Cheetham, A. K. *J. Phys.-Condens. Mat.* **2013**, 25, 395403.
- (31) Kunal, K.; Robertson, C. G.; Pawlus, S.; Hahn, S. F.; Sokolov, A. P. *Macromolecules* **2008**, 41, 7232.
- (32) du Bourg, L. B.; Ortiz, A. U.; Boutin, A.; Coudert, F. X. *Appl Materials* **2014**, 2.
- (33) Yue, Y. Z.; von der Ohe, R.; Jensen, S. L. *J Chem Phys* **2004**, 121, 11508.
- (34) Wang, L. M.; Velikov, V.; Angell, C. A. *J Chem Phys* **2002**, 117, 10184.
- (35) Dudowicz, J.; Freed, K. F.; Douglas, J. F. *J. Phys. Chem. B* **2005**, 109, 21350.
- (36) Angell, C. A.; Moynihan, C. T.; Hemmati, M. *J Non-Cryst Solids* **2000**, 274, 319.
- (37) Doss, A.; Hinze, G.; Schiener, B.; Hemberger, J.; Bohmer, R. *J Chem Phys* **1997**, 107, 1740.
- (38) Greaves, G. N.; Greer, A. L.; Lakes, R. S.; Rouxel, T. *Nat. Mater.* **2011**, 10, 823.
- (39) Goesten, M. G.; Stavitski, E.; Pidko, E. A.; Gucuyener, C.; Boshuizen, B.; Ehrlich, S.; Hensen, E. J. M.; Kapteijn, F.; Gascon, J. *Chem.-Eur. J.* **2013**, 19, 7809.
- (40) Allan, P. K.; Chapman, K. W.; Chupas, P. J.; Hriljac, J. A.; Renouf, C. L.; Lucas, T. C. A.; Morris, R. E. *Chem. Sci.* **2012**, 3, 2559.
- (41) Cliffe, M. J.; Wan, W.; Zou, X. D.; Chater, P. A.; Kleppe, A. K.; Tucker, M. G.; Wilhelm, H.; Funnell, N. P.; Coudert, F. X.; Goodwin, A. L. *Nat Commun* **2014**, 5, 4176.
- (42) Keen, D. A.; Goodwin, A. L. *Nature* **2015**, 521, 303.
- (43) Bennett, T. D.; Cheetham, A. K. *Acc. Chem. Res.* **2014**, 47, 1555.
- (44) Farrow, C. L.; Juhas, P.; Liu, J. W.; Bryndin, D.; Bozin, E. S.; Bloch, J.; Proffen, T.; Billinge, S. J. L. *J. Phys.-Condens. Mat.* **2007**, 19, 335219.
- (45) Wright, A. C. *J Non-Cryst Solids* **1994**, 179, 84.
- (46) Baxter, E.; Bennett, T. D.; Mellot-Draznieks, C.; Gervais, C.; Blanc, F.; Cheetham, A. K. *Phys Chem Chem Phys* **2015**, 17, 25191.
- (47) Solum, M. S.; Altmann, K. L.; Strohmeier, M.; Berges, D. A.; Zhang, Y. L.; Facelli, J. C.; Pugmire, R. J.; Grant, D. M. *J. Am. Chem. Soc.* **1997**, 119, 9804.
- (48) Haines, J.; Levelut, C.; Isambert, A.; Hebert, P.; Kohara, S.; Keen, D. A.; Hammouda, T.; Andrault, D. *J. Am. Chem. Soc.* **2009**, 131, 12333.
- (49) Keen, D. A.; Goodwin, A. L.; Tucker, M. G.; Hriljac, J. A.; Bennett, T. D.; Dove, M. T.; Kleppe, A. K.; Jephcoat, A. P.; Brunelli, M. *Phys. Rev. B* **2011**, 83.
- (50) Tan, J. C.; Cheetham, A. K. *Chem. Soc. Rev.* **2011**, 40, 1059.
- (51) Atanacio, A. J.; Latella, B. A.; Barbé, C. J.; Swain, M. V. *Surface and Coatings Technology* **2005**, 192, 354.
- (52) Mauro, J. C.; Yue, Y. Z.; Ellison, A. J.; Gupta, P. K.; Allan, D. C. *Proc. Natl. Acad. Sci. U.S.A.* **2009**, 106, 19780.
- (53) Wharmby, M. T.; Henke, S.; Bennett, T. D.; Bajpe, S. R.; Schwedler, I.; Thompson, S. P.; Gozzo, F.; Simoncic, P.; Mellot-Draznieks, C.; Tao, H.; Yue, Y. Z.; Cheetham, A. K. *Angew. Chem. Int. Ed.* **2015**, 54, 6447.
- (54) Soper, A. K. *Tech. Rep. RAL-TR-2011-013* **2011**.
- (55) Keen, D. A. *J Appl Crystallogr* **2001**, 34, 172.
- (56) Soper, A. K.; Barney, E. R. *J Appl Crystallogr* **2011**, 44, 714.
- (57) Macrae, C. F.; Bruno, I. J.; Chisholm, J. A.; Edgington, P. R.; McCabe, P.; Pidcock, E.; Rodriguez-Monge, L.; Taylor, R.; van de Streek, J.; Wood, P. A. *J Appl Crystallogr* **2008**, 41, 466.
- (58) Oliver, W. C.; Pharr, G. M. *J Mater Res* **2004**, 19, 3.
- (59) Fung, B. M.; Khitrin, A. K.; Ermolaev, K. *J Magn Reson* **2000**, 142, 97.
- (60) Morcombe, C. R.; Zilm, K. W. *J Magn Reson* **2003**, 162, 479.
- (61) Bertani, P.; Raya, J.; Bechinger, B. *Solid State Nucl. Magn. Reson.* **2014**, 61-62, 15.
-